Characterization of the JPE Hexapod for Quantum Optics

THESIS

submitted in partial fulfillment of the
requirements for the degree of

BACHELOR OF SCIENCE
in
PHYSICS

Author :	Tomas T. Osterholt
Student ID :	1822276
Supervisor :	Prof. Dr. Martin P. van Exter
2^{nd} corrector :	Dr. Milan P. Allan

Leiden, The Netherlands, January 25, 2020

Characterization of the JPE Hexapod for Quantum Optics

Tomas T. Osterholt

Huygens-Kamerlingh Onnes Laboratorium, Universiteit Leiden
P.O. Box 9500, 2300 RA Leiden, The Netherlands

January 25, 2020

Abstract

The hexapod made by Janssen Precision Engineering (JPE) is tested for optical purposes. Equations describing the movements of the platform are derived and tested using interferometric techniques and imaging systems. A Python program for the hexapod motion control is developed and implemented, and its limitations are discussed. Several technical features, most notably the piezo actuators of the hexapod, are examined.

Contents

Version of January 25, 2020– Created January 25, 2020 - 10:44

Chapter 1

Introduction

In the last decade, the interest in interactions between matter on the atomic or molecular scales and optical resonators has significantly increased [1] [2] [3]. Using so-called microcavities, consisting of two mirrors at most a few micrometers apart, one is able to observe several unique quantum phenomena, of which the Purcell effect is the most prominent [4].

Building these cavities, however, is far from trivial; for not only are the mirrors required to be aligned within nanometer precision, a positional stability in the (sub)nanometer regime is needed as well [2] [3].

One of the devices that can (partially) meet these requirements is the hexapod of Janssen Precision Engineering (JPE). In our research we will focus our attention on the movements of the movable hexapod platform. We use the geometry of the system to derive equations describing its motion and test these using both a Michelson interferometer and a basic imaging setup. We will also discuss several technical features of the JPE hexapod, turning our attention mainly to the piezo actuators used for the platfrom movements. Most importantly, we will develop a program with which the motion of the hexapod can be controlled, in the meantime also considering its limitations. Lastly, we will suggest several improvements which can be made to our characterization experiments and provide a helpful guide to using the hexapod.

Version of January 25, 2020– Created January 25, 2020 - 10:44

Chapter 2

Theoretical Considerations

Before we discuss our experiments, we deem it necessary to briefly review the relevant physical concepts and provide a solid theoretical framework for our project.

In the course of our research we made extensive use of the Michelson interferometer, which we will describe in some detail here. Furthermore, we will provide a short summary of the basic properties and working principles of the JPE hexapod.

2.1 The Michelson interferometer

Invented by Albert Abraham Michelson in the late nineteenth century, and most famously employed in his experiment with Edward Morley in 1887 to detect the existence of the aether, the Michelson interferometer is widely used today in the fields of optics and spectroscopy. Taking advantage of path length differences between different light rays from a coherent light source to create interference patterns, the Michelson interferometer can be applied to measure either wavelengths or physical displacements with a remarkably high precision [5]. With the advent of the laser the accuracy and ease of using the Michelson interferometer improved even further, and it is now considered an indispensable tool in modern physics research, as evidenced by its successful application in the detection of gravitational waves in 2015 [6]. Common setups for the modern Michelson interferometer are drawn in Figures 2.1 and 2.2 .

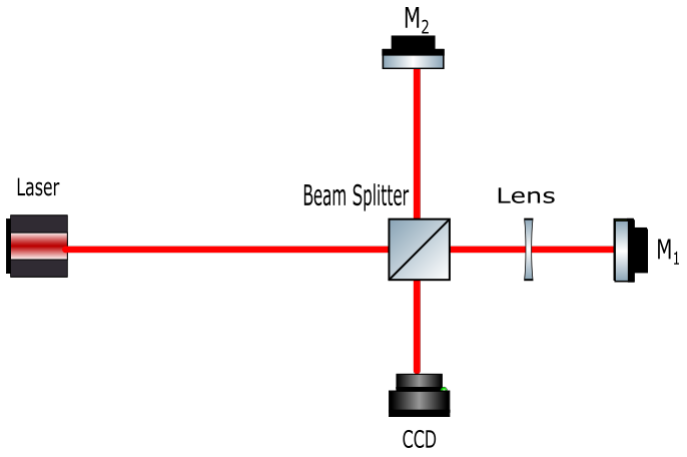

Figure 2.1: *A modern setup of the Michelson interferometer; particulary well-suited for creating circular fringe patterns.*

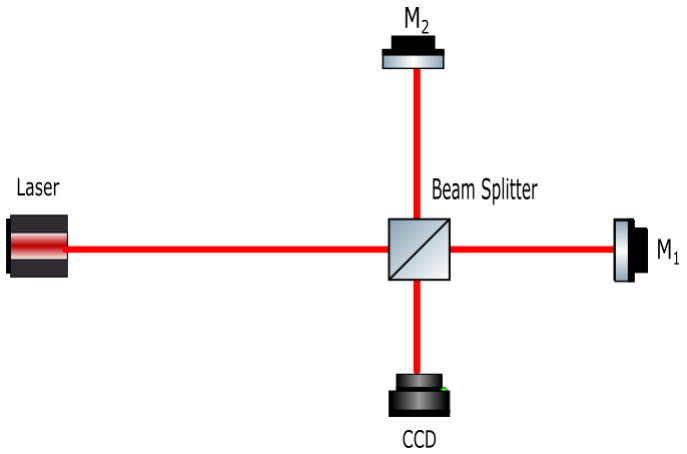

Figure 2.2: *A modern setup of the Michelson interferometer: particularly well-suited for creating Fizeau fringes.*

Using either one of these setups as a reference, the principle idea of the Michelson interferometer is fairly easy to grasp. A light wave from a quasi-monochromatic source, in our case a laser, is divided in two by the beam splitter, with one part going straight ahead towards mirror M_1, and the other part proceeding in the orthogonal direction, towards mirror M_2 [7]. After reflection from the mirrors parts of the reflected waves pass through the beam splitter, and travel towards the detector, where they interfere with one another [7]. One can create several different types of interference patterns with the Michelson interferometer, of which two will be discussed here.

2.1.1 Circular fringes

We first consider circular fringe patterns, such as the one shown in Figure 2.3. These patterns can be created with the setup of Figure 2.1. It is fairly straightforward to understand how this pattern is formed. The lens in the M_1-arm curves the (approximately) plane light waves coming from the laser, turning them into (approximately) spherical waves, whereas the waves travelling towards M_1 stay planar. At the detector the plane and spherical waves interfere with one another, resulting in a circular fringe pattern, as can be seen from symmetry.

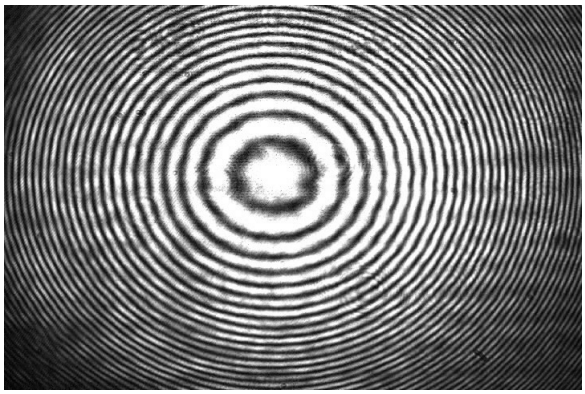

Figure 2.3: *Circular fringes created by a Michelson interferometer during the course of one of our hexapod characterization experiments on 14 November 2019.*

In our experiments we are only interested in changes in the center of this interference pattern resulting from the movement of the mirror M_2 along the direction of the incident laser beam there.

To understand what happens, we first note that in the center of the pattern the spherical wave can be described as a plane wave [8]. Using the interference principle, we then see that a displacement Δd of mirror M_2 will result in a fringe shift of [8] [9]

$$\Delta m = \frac{2\Delta d}{\lambda}, \tag{2.1}$$

where Δm is the amount of fringes passing through the center, and where λ is the wavelength of the light. Conversely, this relation allows us to determine Δd by simply counting how many fringes have passed along a central point, a fact which we will use in our experiments.

2.1.2 Fizeau fringes

The second type of fringes we will consider are known as Fizeau fringes, and are shown in Figure 2.4. They can most easily be created using the setup of Figure 2.2. We note that there are no lenses used in this setup, for reasons which will become clear in the following discussion.

Now, an observer positioned at the detector will simultaneously see mirrors M_1 and M_2 in the beam splitter [7]. This allows us to redraw the interferometer as if all the elements were in a straight line [7], as shown in Figure 2.5. Note that M_1' corresponds to the image of mirror M_1 in the beam splitter [7]. As seen in the figure, the mirrors are inclined with respect to each other, making a *small* angle α [5][7], and we immediately see that the fringe separation distance Δx between two consecutive fringes is given by [7]:

$$\Delta x = \frac{\lambda}{2\alpha}. \tag{2.2}$$

Defining our x- and y-axes as being orthogonal to each other and to the z-axis, as defined previously, we can use this formula to determine small angular displacements around these axes, which we will use in some of the hexapod characterization experiments.

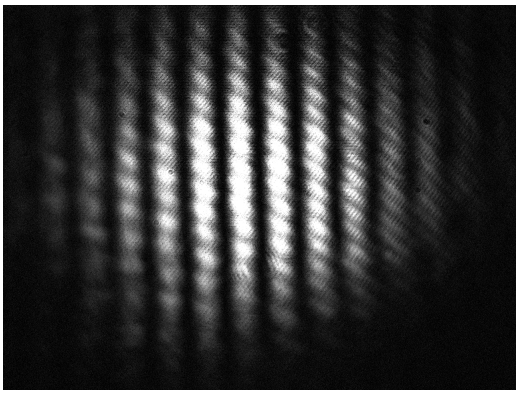

Figure 2.4: *Vertical Fizeau fringes created by a Michelson interferometer in the course of one of our hexapod characterization experiments on 16 December 2019.*

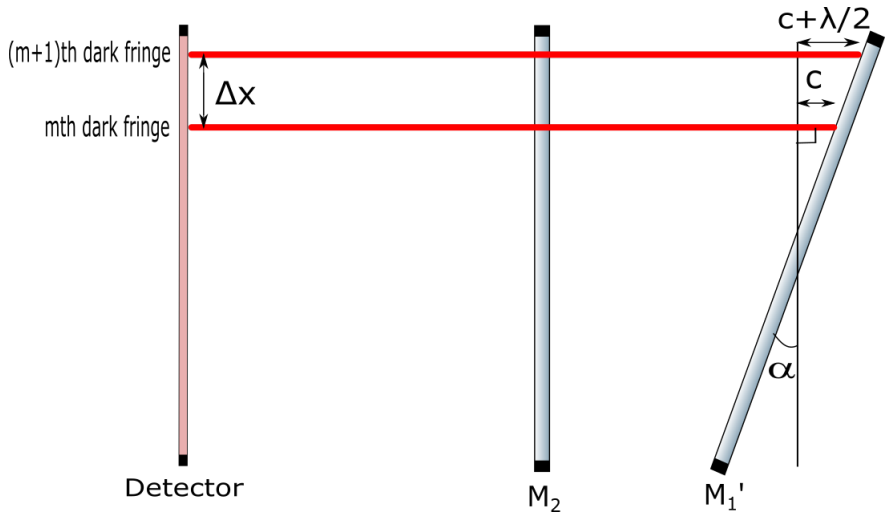

Figure 2.5: *Sketch of the origin of the Fizeau fringes. Here the fringes will be parallel to the line orthogonal to the plane in the figure.*

2.2 Outline of the JPE hexapod

Having discussed the Michelson interferometer rather thoroughly, we will now provide a short summary of the basic properties of the JPE hexapod. For a more detailed description we advise the reader to contact Janssen Precision Engineering.

2.2.1 Working principle

As can be seen from the technical drawing of the hexapod, made by Harmen van der Meer of the Fijnmechanische Dienst and shown in Figure 2.6, the hexapod consists of a platform with six legs, which can effectively be expanded or contracted using the six piezo motors (or actuators) placed there. Note that we have added the word ”effectively” to indicate that the length of the legs itself stays fixed, but their effective length changes when the motors either push the ends of the legs upwards or pull them downwards with respect to the base plane. Since each leg can in principle move separately from all others, the movable platform has a total of six degrees of freedom.

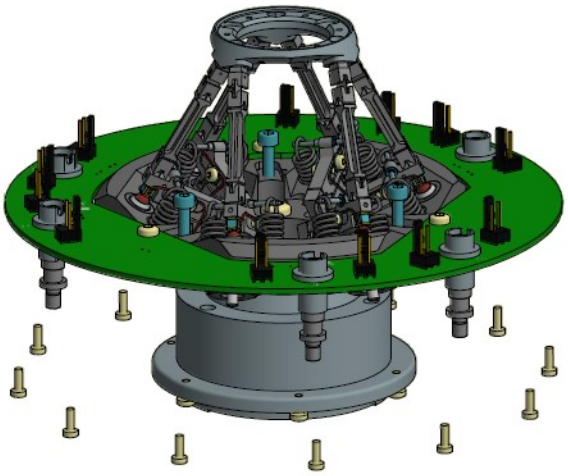

Figure 2.6: *A technical drawing of the JPE Hexapod made by Harmen van der Meer. The upper platform, connected to the six legs, is the movable platform of the hexapod. The plane surrounded by the green ring is the base plane (or base platform).*

The basic working principle of the piezo actuators can be considered as the electric equivalent of the stick-slip effect [10]. A ”fast” voltage pulse is sent to rapidly expand the piezo, and is then followed by a ”slow” voltage pulse to contract it gradually. The combined effect of this pulse train are very small net contractions or expansions. We refer to these net displacements as motor steps. It should be noted that piezo's are subjected to the effect of hysteresis [11], which in practice means that the actual size of a single motor step is rather unpredictable.

The hexapod also contains optical readers, which essentially provides us with a kind of ruler to determine the position of a leg (with respect to some predefined origin). We will often refer to the distance between two consecutive markers of the optical readers as an optical step. In general, several motor steps are required to travel one optical step.

2.2.2 Electronical aspects

Before deriving the platform displacement equations, we give a very brief sketch of the electronics underlying the hexapod, with a particular focus on the external driver which is used to generate the voltage pulses.

According to ing. Arno van Amersfoort of the Electronics Department, the driver-piezo circuit can be considered analogous to the electric circuit

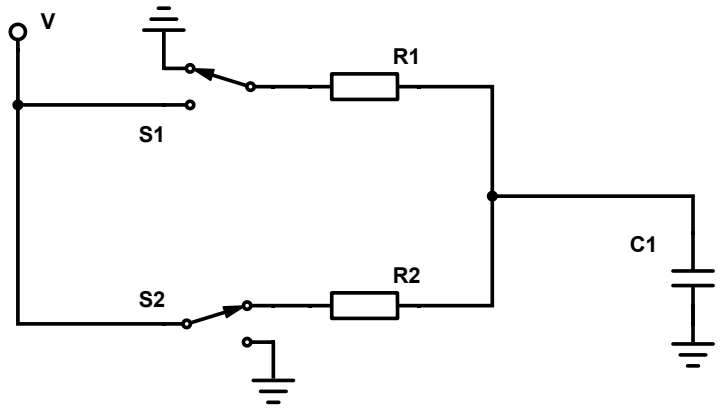

Figure 2.7: *Drawing of a circuit analogous to the driver-piezo circuit used for the hexapod control. Here C1 refers to the piezo, which is essentially a capacitor. In our particular setup we have R1 equal to 18 Ω and R2 $\sim$ 2 kΩ. The capacitance of the piezo is not known.*

shown in Figure 2.7. The actual circuit, of course, is far more complex, containing electronic elements not shown here, including transistors. Focusing on this figure, we note that there are two switches in this circuit, conveniently named S1 and S2. When the "fast" voltage pulse is sent, S1 is closed and S2 is open. When the "slow" voltage pulse is sent, it is the other way around. Note that, according to Arno, the circuit is designed in such a way that the "fast" and "slow" pulses are almost each others mirror image (with respect to the voltage axis); whereas the "fast" pulse starts with a sharp rise in the voltage followed by a slow decline, the "slow" pulse rises slowly in the voltage first to decline sharply afterwards. They are, however, not exactly mirrored, for then the net displacement of the piezo would equal zero. By changing the resistors, one can alter the pulses in such a way that the pulses become either more or less 'similar' (more meaning they increasingly resemble mirror images), which corresponds to smaller or bigger average motor steps respectively. For more details, we suggest the reader to contact Arno.

Chapter 3

Calculation of Platform Displacements

We will now describe the geometry of the JPE hexapod and the movement of the platform under expansion/contraction of the six legs of the hexapod. This description is based on a single A4 document that JPE provides on their website and on technical drawings that Harmen van der Meer made from a 3D-drawing that he received from JPE. We have added the mathematical framework to this description.

3.1 Geometry and parameters

Referring to Figure 3.1 the situation can be described as follows: There are six legs, all connected to a circle of radius R_B on a base. The base defines the $z = 0$ plane; the center of the base circle defines the origin. The upper ends of the legs are connected to a circle of radius R_P on a platform. In its 'rest position' this platform is located in the $z = z_P$ plane. The in-plane positions of the six legs on each circle are characterized by an angle: $\alpha_B > 60^\circ$ for the base and $\alpha_P < 60^\circ$ for the platform. The connection of each leg to the base and platform is modeled as if it is flexible, like a ball or point contact.

Figure 3.1 also shows the labeling of the end points of the six legs: $P_{B1} - P_{B6}$ for the lower ends on the base circle and $P_{P1} - P_{P6}$ for the upper ends on the platform circle. We will perform most of our analysis on leg 1 and use symmetry arguments to relate these results to the other five legs. The position of the lower end of leg 1 on the base circle is characterized by the angle $\alpha_B/2$ that it makes with the negative y-axis. The position of the

upper end of leg 1 on the platform circle is characterized by a similar angle $\alpha_P/2$.

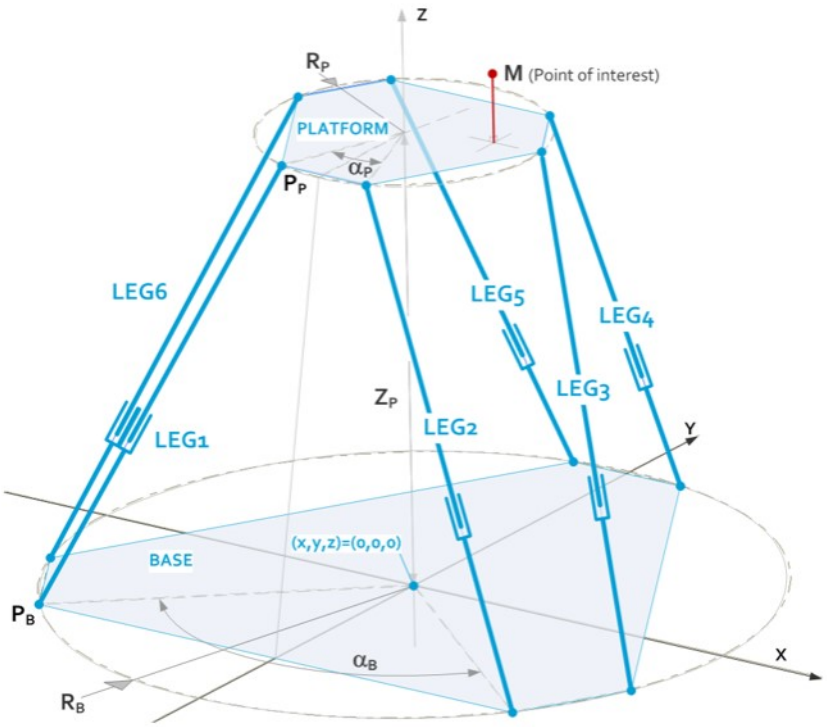

Figure 3.1: *Geometry of the JPE hexapod in three dimensions. This figure was provided by JPE.*

It is convenient to introduce the following additional parameters:

- $s = \sqrt{s_\perp^2 + {s_\parallel}^2}$ is the length of *each* leg in its rest position.
- $s_\perp = z_P$ is the projection of the leg on the vertical direction, denoted as $\perp$ to indicate that it is perpendicular to the base plane.
- $s_\parallel$ is the projection of the leg on the base plane; $s_\parallel$ has a direction and is actually a vector $\mathbf{S}_\parallel$.
- β is the angle between the projected base vector $\mathbf{P}_{Bi}$ and the projected leg $\mathbf{S}_i \equiv \mathbf{P}_{Pi} - \mathbf{P}_{Bi}$, where $i = 1, 2, \ldots, 6$. This angle is shown in Figure 3.2.
- φ is the angle between vector $\mathbf{S}_i$ and the base plane, such that $\sin\varphi = s_\perp/s$ and $\cos\varphi = s_\parallel/s$.

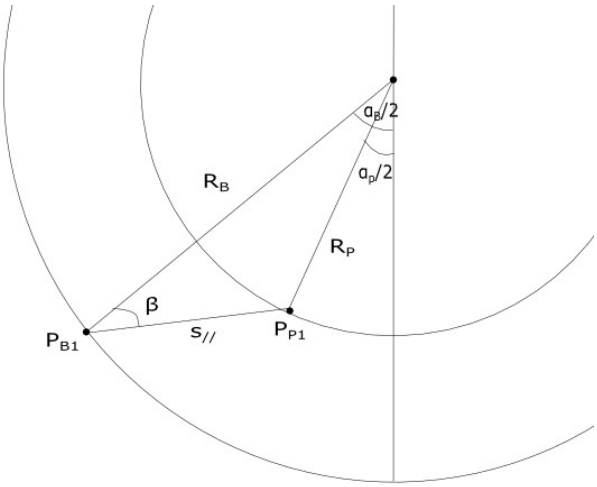

Figure 3.2: *Projection of the movable platform on the base plane. Several of the important parameters are shown.*

3.2 Preliminary calculations

The length of each leg in rest follows from simple vector algebra. We can for instance use the rest positions of the end points of a leg to write $\mathbf{S}_1 \equiv \mathbf{P}_{P1} - \mathbf{P}_{B1} = ((R_B \sin\alpha_B/2 - R_P \sin\alpha_P/2), (R_B \cos\alpha_B/2 - R_P \cos\alpha_P/2), z_P)$ as a 3D vector and calculate its length. We can also start from $s_\perp = z_P$ and use the projected triangle in Figure 3.2 to find the projected length $s_\parallel$ via the cosine rule

$$s_\parallel{}^2 = R_B^2 + R_P^2 - 2R_B R_P \cos\left[(\alpha_B - \alpha_P)/2\right] \tag{3.1}$$

Starting from the symmetric rest position, we will derive the effect of six fundamental displacement and rotation operations on the vector positions of all end points $\mathbf{P}_i \equiv \mathbf{P}_{Pi}$ for i = 1, ... , 6. (base positions are fixed). We consider only small movements $d\mathbf{P}_i$ of the platform points and use first-order Taylor expansions when needed. The corresponding effective length changes of the six legs follow by projection:

$$ds_i = \frac{\mathbf{S}_i \cdot d\mathbf{P}_i}{s_i} = \sin\varphi \; dP_{i,\perp} + \cos\varphi \cos\chi_i \; dP_{i,\parallel} \tag{3.2}$$

where χ_i is the angle between the in-plane $\mathbf{S}_{i,\parallel}$ and in-plane movement $d\mathbf{P}_{i,\parallel}$.

3.3 Six basic operations

We will consider six basic displacement operations: translations in x, y, z and rotations θ_x, θ_y, θ_z.

To find the leg displacements corresponding to those operations we first note that that the symmetry group of the hexapod configuration contains, among other things, the 120°-rotations around the z-axis and the reflections in the yz-plane. By considering the effect of these symmetry transformations on the operations themselves, one can then find the interrelations between the leg displacements. For example, the reflection in the yz-plane shows that the translation in y yields $ds_1 = ds_2$, $ds_3 = ds_6$ and $ds_5 = ds_4$.

To find the expressions for the ds_i in terms of the parameters mentioned in 3.1 we then use basic Euclidean plane geometry. Several helpful figures for deriving the following results have been included in Appendix A.

1. z **= translation in z-direction**
   Displaces all platform points by the same amount $dP_{i,\perp} = dz$ (no in-plane movement). The corresponding changes in the leg lengths are all equal:

$$ds_1 = ds_2 = ds_3 = ds_4 = ds_5 = ds_6 = \sin\varphi \, dz \tag{3.3}$$

2. θ_z = **rotation around z-axis**
   Displaces all platform points by the same amount $dP_{i,\parallel} = R_P d\theta_z$ in the tangential direction (no out-of-plane movement). The corresponding change in the leg length depends on $\cos\varphi$, via the in-plane projection, and on the angle $\chi_1 = \beta + (\alpha_B - \alpha_P)/2$ between the tangential displacement $d\mathbf{P}_{i,\parallel}$ and the projected leg $\mathbf{S}_{i,\parallel}$ via:

$$\begin{aligned} ds_1 = -\, ds_2 = ds_3 = -\, ds_4 = ds_5 = -\, ds_6 = \\ = \cos\varphi \sin\left[\beta + (\alpha_B - \alpha_P)/2\right] R_P d\theta_z = \cos\varphi \frac{R_B}{s_\parallel} \sin\left[(\alpha_B - \alpha_P)/2\right] R_P d\theta_z \end{aligned} \tag{3.4}$$

   where we used the law of sines to obtain the final equation.

3. y = **translation in y-direction**
   Displaces all platform points by the same amount $dP_{i,\parallel} = dy$ in the (in-plane) y-direction (no out-of-plane movement). The corresponding changes in the leg length are $ds_i = \cos\varphi \cos\chi_i dP_{i,\parallel}$, where the

angle χ_i between $\mathbf{S}_{i\|}$ and $d\mathbf{P}_{i\|}$ is different for the different i's, such that:

$$\begin{aligned} ds_1 = \quad ds_2 = \quad & \cos\varphi\ \cos\left(-\beta-\alpha_B/2\right)\ dy = \quad \cos\varphi\ \cos\left(\beta+\alpha_B/2\right)\ dy \\ ds_3 = \quad ds_6 = \quad & \cos\varphi\ \cos\left(\beta+\alpha_B/2-120^\circ\right)\ dy \\ ds_5 = \quad ds_4 = \quad & \cos\varphi\ \cos\left(\beta+\alpha_B/2+120^\circ\right)\ dy \end{aligned} \tag{3.5}$$

where we have added the first (double) equation to show that the angle of $\mathbf{S}_1 \equiv \mathbf{P}_{P1} - \mathbf{P}_{B1}$ with the positive y-axis is defined in the usual way.

4. θ_y **= rotation around** y**-axis**
Displaces all platform points in the out-of-plane direction by an amount $dP_{i,\perp} \propto R_P d\theta_y$ that scales with distance from the y-axis (no in-plane movement). The corresponding changes in the leg length are:

$$\begin{aligned} ds_1 = \quad -ds_2 = \quad & -\sin\varphi\ \sin\left(-\alpha_P/2\right)\ R_p\ d\theta_y = \quad \sin\varphi\ \sin\left(\alpha_P/2\right)\ R_p\ d\theta_y \\ ds_3 = \quad -ds_6 = \quad & \sin\varphi\ \sin\left(\alpha_P/2-120^\circ\right)\ R_p\ d\theta_y \\ ds_5 = \quad -ds_4 = \quad & \sin\varphi\ \sin\left(\alpha_P/2+120^\circ\right)\ R_p\ d\theta_y \end{aligned} \tag{3.6}$$

5. x **= translation in** x**-direction**
Displaces all platform points by the same amount $dP_{i,\|} = dx$ in the (in-plane) x-direction (no out-of-plane movement). The corresponding changes in the leg length are:

$$\begin{aligned} ds_1 = \quad -ds_2 = \quad & \cos\varphi\ \cos\left(90^\circ-\beta-\alpha_B/2\right)\ dx = \quad \cos\varphi\ \sin\left(\beta+\alpha_B/2\right)\ dx \\ ds_3 = \quad -ds_6 = \quad & \cos\varphi\ \sin\left(\beta+\alpha_B/2-120^\circ\right)\ dx \\ ds_5 = \quad -ds_4 = \quad & \cos\varphi\ \sin\left(\beta+\alpha_B/2+120^\circ\right)\ dx \end{aligned} \tag{3.7}$$

6. θ_x **= rotation around** x**-axis**
Displaces all platform points in the out-of-plane direction by an amount $dP_{i,\perp} \propto R_P d\theta_x$ that scales with distance from the x-axis (no in-plane movement). The corresponding changes in the leg length are:

$$\begin{aligned} ds_1 = \quad ds_2 = \quad & -\sin\varphi\ \sin\left(90^\circ-\alpha_P/2\right)\ R_p\ d\theta_x = \quad -\sin\varphi\ \cos\left(\alpha_P/2\right)\ R_p\ d\theta_x \\ ds_3 = \quad ds_6 = \quad & -\sin\varphi\ \cos\left(\alpha_P/2-120^\circ\right)\ R_p\ d\theta_x \\ ds_5 = \quad ds_4 = \quad & -\sin\varphi\ \cos\left(\alpha_P/2+120^\circ\right)\ R_p\ d\theta_x \end{aligned} \tag{3.8}$$

Finally, we note that operation 5 (displacement in x-direction) can also be synthesized from two modified displacement in the y-direction, using the following trick: (i) create the two operations for displacement along axes oriented at $\pm 120^\circ$ with respect to the y-axis, (ii) subtract these two operations, (iii) divide by $\sqrt{3}$ to obtain the sought-for x-displacement. Likewise, operation 6 (rotation around x-axis) can be synthesized from two two rotations around the 'y $\pm 120^\circ$' axes. We have performed both syntheses and checked that the result are the same as the ones mentioned above.

3.4 Checks and symmetries

Looking back at the obtained results we note that:

- The three operations z, θ_x, and θ_y displace the end points in the out-of-plane direction and therefore scale with $\sin\varphi = s_\perp/s$, whereas the three operations θ_z, x and y displace the end points in-plane and therefore scale with $\cos\varphi = s_\parallel/s$.

- The operations z, y and θ_x are even/symmetric under reflection in the yz mirror plane, whereas the operations θ_z, θ_y and x are odd/anti-symmetric under this mirror operation.

- We had expected that the six operations are orthogonal to each other, i.e. that the six-element displacement vector $\mathbf{s}_{A'}$ of any base operation A' is orthogonal to the displacement vector $\mathbf{s}_{B'}$ of any other base operations B'. We checked this. We found that any even operation is naturally orthogonal to any odd operation due to the relation:

$$\cos(\gamma) + \cos(\gamma + 120^\circ) + \cos(\gamma - 120^\circ) = 0\,, \tag{3.9}$$

  which applies for any angle γ and is also valid when the cosine function is replaced by the sine function. However, the orthogonality between $\mathbf{s}_y$ and $\mathbf{s}_{\theta_y}$ is only satisfied when $\cos(\beta + \alpha_B/2 - \alpha_P/2) = 0$. For the set of the three odd vectors, two of the three orthogonality relations are again satisfied by the above relation. Yet the orthogonality between $\mathbf{s}_x$ and $\mathbf{s}_{\theta_x}$ is now only satisfied when $\sin(\beta + \alpha_B/2 - \alpha_P/2) = 0$. Hence we find that the complete set of six basis operations is **not** orthogonal. We do not understand why this is so.

Version of January 25, 2020– Created January 25, 2020 - 10:44

3.5 Matrix formulation

All the relations derived in Section 3.3 can be succinctly summarized in matrix form, yielding the equation

$$A\Delta\mathbf{r} = \Delta\mathbf{s}, \tag{3.10}$$

where we have $\Delta\mathbf{r} = [dx, dy, dz, d\theta_x, d\theta_y, d\theta_z]^T$, $\Delta\mathbf{s} = [ds_1, ds_2, ds_3, ds_4, ds_5, ds_6]^T$, and A the 'Cartesian-to-leg' transformation matrix. Here T refers to the transpose operation, since $\Delta\mathbf{r}$ and $\Delta\mathbf{s}$ are column vectors. A is a 6x6 matrix whose columns can directly be found from the equations in Section 3.3. For instance, the fifth column vector, corresponding to θ_y, of A is simply given by $[a, -a, b, -c, c, -b]^T$, with $a = \sin\varphi \sin(\alpha_P/2) R_p$, $b = \sin\varphi \sin(\alpha_P/2 - 120^\circ) R_p$ and $c = \sin\varphi \sin(\alpha_P/2 + 120^\circ) R_p$.

We can also consider inverting Equation 3.10, obtaining Δr from $\Delta\mathbf{s}$:

$$\Delta\mathbf{r} = \tilde{A}\Delta\mathbf{s}, \tag{3.11}$$

where $\tilde{A}$ is the inverse matrix of A. The inverse $\tilde{A}$ can readily be found by using the quasi-orthogonality of the column vectors of A together with the Gram-Schmidt theorem [12]. We will, however, not go over the details here.

3.6 Practical aspects

The 3D-drawings show that the connection of each leg to the base and platform is not a simple ball or point contact, but actually comprises two 2D joints that bend in orthogonal directions. For simplicity, we will treat each pair of joints as a single point contact at the average position. Figure 3.3 shows that the associated parameters are $R_B = \frac{31.59+33.15}{2}$ mm $= 32.37$ mm, $R_P = \frac{21.65+19.83}{2}$ mm $= 20.74$ mm, and $z_P = 22.91$ mm. Figure 3.4 shows that the average angular positions correspond to $\alpha_B = 120^\circ - 60.83^\circ = 59.17^\circ$ and $\alpha_P = 120^\circ - 85.83^\circ = 34.17^\circ$. Substitution of these parameters in Eq. (3.1) yields $s_\parallel = 12.94$ mm and $s = 26.31$ mm, making $\sin\varphi = 0.871$ and $\cos\varphi = 0.491$. The angle β can be found with the law of sines. Specifically, $\sin(\beta) = \frac{R_P}{s_\parallel} \sin((\alpha_B - \alpha_P)/2) = 0.347$.

Version of January 25, 2020– Created January 25, 2020 - 10:44

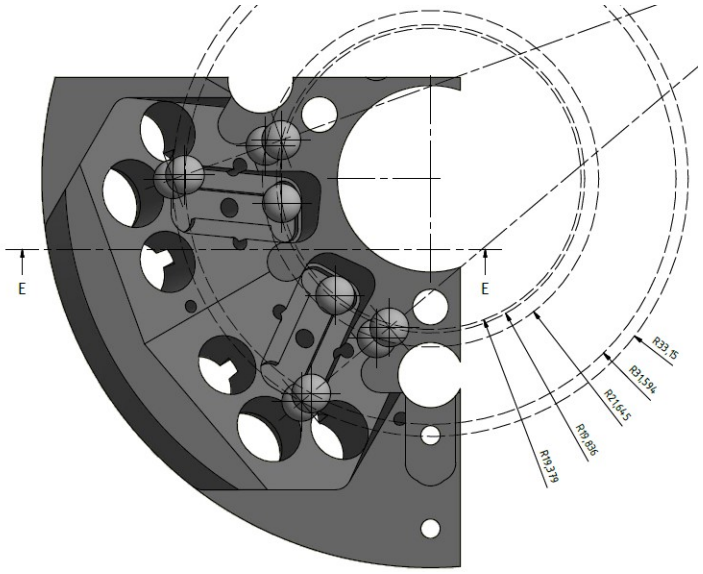

Figure 3.3: *Technical drawing, by Harmen van der Meer, of the hexapod platforms, showing the different platform radii.*

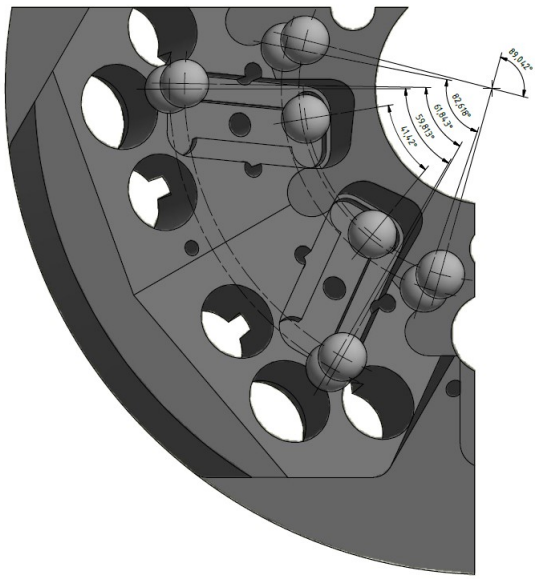

Figure 3.4: *Technical drawing, by Harmen van der Meer, of the hexapod platforms, showing the different platform angles.*

Figure 3.5 shows the mechanism used to change the effective leg length. In the two planes set by the 2D joint these arm lengths are virtually identical at 26.8 mm and 26.78 mm, respectively. This is somewhat larger than

the value $s = 26.31$ mm mentioned above, maybe due to the double-joint construction. Furthermore, the leg length doesn't really change, but the bottom part of the leg is pushed upwards or downwards via a lever with a range of 1.5-2.0 mm.

Finally, we note that the top of the platform is located $h = 15 - 16$ mm above the middle of the six pairs of upper joints (exact height difficult to judge from figure). This elevated location will not affect the z and θ_z operations, and the x and y displacements also remain pure. However, the $\Delta\theta_y$ rotation will now also produce an extra displacement $\Delta x = h\Delta\theta_y$. Likewise, the $\Delta\theta_x$ rotation will now produce an extra displacement $\Delta y = -h\Delta\theta_x$. These couplings can be removed by subtracting the spill-overs from the original rotation operations, thus resulting in two modified pure rotation operators.

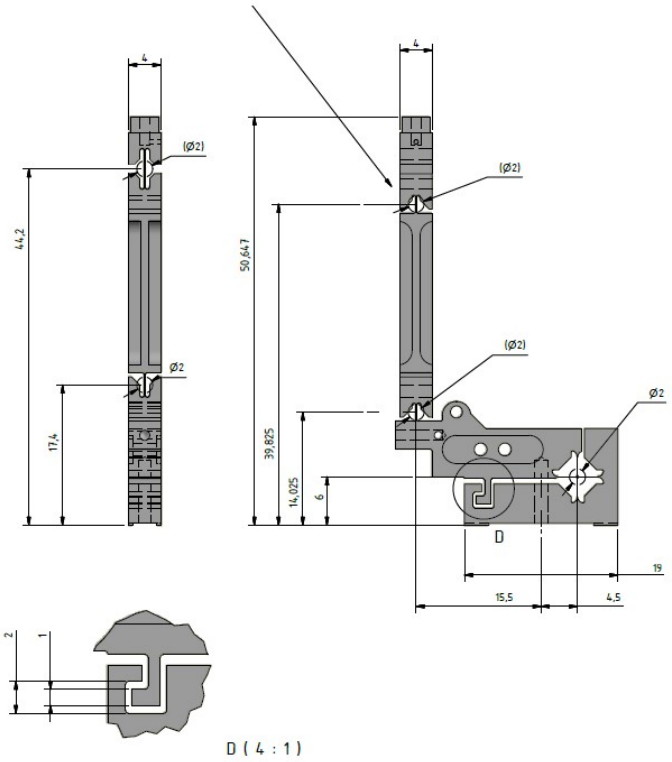

Figure 3.5: *Technical drawing, by Harmen van der Meer, of the hexapod joints and the leg displacement mechanism.*

Chapter 4

Hexapod Control

In this chapter we describe the hexapod control program, which we use to move the platform. We also discuss several characteristic features of the piezo actuators, as well as a method to decrease the average motor step size.

4.1 Hexapod control program

Together with ing. Arno van Amersfoort we made a program to control the movements of the hexapod platform. A picture of the user interface of this program is included as Figure 4.1.

The upper left block shows the current leg positions $\mathbf{s}_{now}$ in terms of optical steps. Note that these leg positions are defined with respect to some 'origin' position which was set by Arno. The hexapod remembers this origin position, even after turning the program on and off. For more details we refer the reader to Arno.

The upper right block gives the current platform position $\mathbf{r}_{now}$ with respect to some reference position, which need not be the origin (the user can choose any possible leg position as a reference point), in terms of the Cartesian coordinate set $\{x, y, z, \theta_x, \theta_y, \theta_z\}$. The Cartesian coordinates are directly calculated from the leg positions, or, stated more accurately, from the difference between the current leg positions $\mathbf{s}_{now}$ and the leg positions of the reference position $\mathbf{s}_{ref}$. We can neatly summarize this calculation as

$$\mathbf{r}_{now} = \tilde{A}(\mathbf{s}_{now} - \mathbf{s}_{ref}), \tag{4.1}$$

using the terminology of the previous chapter. We haven chosen not to include the possibility of changing the reference position in the interface

itself; this needs to be done directly in the code itself.

In the middle block, the user can change the voltage and the frequency with which pulses are sent to the piezo actuators. Note that for safety reasons the user can only change the voltages to values in-between 35 and 200 V, and the frequencies to values in-between 1 and 600 Hz. According to both JPE and Arno, one can best use voltages of 100 to 130 V and pulse frequencies of 100 to 300 Hz at room temperature. We emphasize that one should be particularly careful with the voltage, as values far above 130V can damage the piezo's.

In the bottom left block the user can insert the Cartesian coordinates he or she wants the platform to have with respect to the reference position. Pressing the Start-button will then result in the platform moving towards the desired position $\mathbf{r}_{desired}$. This can again be stated mathematically as

$$\Delta \mathbf{s}_{needed} = A(\mathbf{r}_{desired} - \mathbf{r}_{now}), \tag{4.2}$$

where $\Delta \mathbf{s}_{needed}$ is the leg displacement vector. The legs will thus move towards $\mathbf{s}_{now} + \Delta \mathbf{s}_{needed}$.

Finally, the bottom right block allows the user to move the legs by individual motor steps, as opposed to optical steps, which can be of use when one needs to fine-tune, for instance, the alignment of the mirrors in a microcavity.

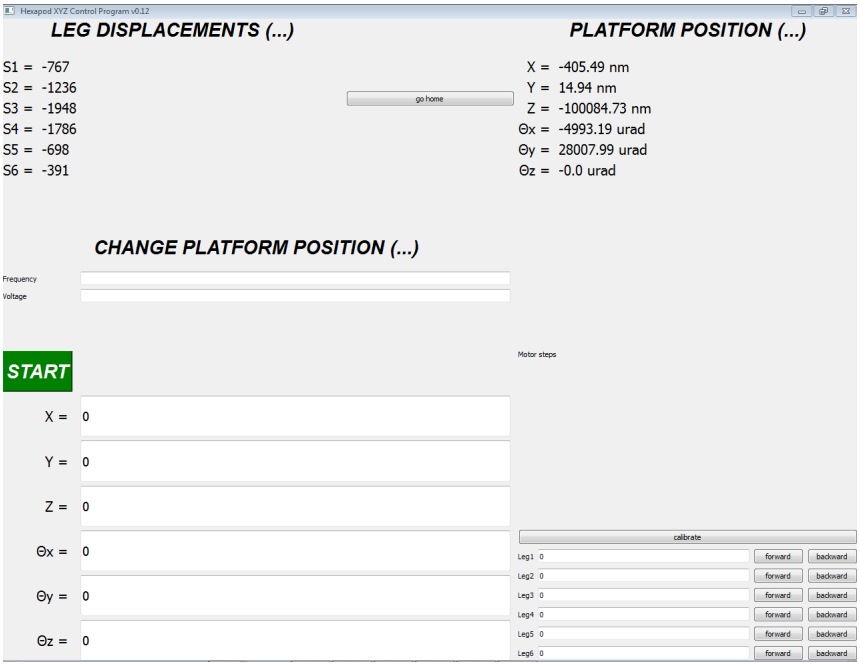

Figure 4.1: *The user interface of the hexapod control program.*

4.1.1 Discreteness of the optical steps

While the mathematics seems relatively straightforward, one should pay attention to the fact that the leg positions are given in terms of optical steps, and therefore can only take on integer values. Of course, it is possible to add individual motor steps, thereby expanding the set of possible positions, but, because of the unpredictability of the step size, one then loses information regarding the actual position of the platform. While this discreteness does not pose a problem for calculating the platform position (in Cartesian coordinates) from the leg positions, at least not when one knows the size of an optical step, the other way around is not trivial. This is because not every Cartesian position corresponds to a possible leg position (due to the integer restriction), whereas every given leg position does have a corresponding Cartesian position.

To deal with this problem we first calculate the amount of optical steps $\Delta\mathbf{s}_{needed}$ needed to go to the desired Cartesian position using Equation 4.2, and then round the entries in $\Delta\mathbf{s}_{needed}$ off to integer values. Note that the upper right block in the user interface will still display the correct Cartesian position after the platform movement, since this is directly calculated from the leg positions.

One notable problem arising from the discreteness of the optical steps is that it is, in general, not possible to reach pure x-, y-, θ_x- and θ_y-positions (with respect to some reference position). To understand why this is the case one needs to consider the column vectors of A corresponding to the mentioned Cartesian coordinates. Ignoring the plus and minus signs, each column contains three different expressions. Filling in the values for the several constants in these expressions, one finds three different numbers for each column, $\{a, b, c\}$, for which there does not exist a number γ such that γa, γb and γc are all integer. This means that there is no $\Delta\mathbf{s}_{needed}$ with only integer entries such that it yields a pure x-, $y-$, θ_x- or θ_y-displacement. Note that this problem does not arise for z- or θ_z-displacements, for then, apart from the plus and minus signs, the columns each contain only one expression.

4.1.2 Important remarks

It is important to note that the origin has been calibrated a total of three times, mainly based on electronical considerations which will not be discussed here. The first calibration, by ing. Arno van Amersfoort, took place around 7 October 2019, a month before our first experimental tests of the hexapod. The second calibration, again by Arno, was carried out around

22 November 2019. During these calibrations information regarding the position of the old origin with respect to the new one was lost.

For the sake of clarity, we will add labels (*a*) and (*b*) to figures of experimental data. Experiments with the label *a* took place before the second calibration, those with label *b* after this date. The leg positions mentioned there are taken relative to the position of the origin at that time.

One would expect that the optical step size is the same regardless of the position, and hence no problems should arise from these calibrations. However, this needs to be tested experimentally, which we will discuss in Chapter 5.

Finally, a third calibration took place in January 2020, by Corné Koks, with the origin now defined as the highest point one can (safely) reach. However, our last experiments took place around the 20th of December, making this calibration irrelevant for the experiments discussed here.

4.2 Typical behaviour of the piezo actuators

While the characteristics of the piezo actuators used are not of great importance for our project, we deem it helpful to provide a very rough sketch of their typical behaviour, most notably their apparent dependence on the leg position.

On the advise of ing. Arno van Amersfoort we altered the circuit discussed in Section 2.2.2 and shown in Figure 2.7 by replacing the 18 Ω resistor with one from 100 Ω. According to Arno, this would then result in a decrease of the average size of a motor step. To check this we used a feature of the hexapod program which allows us to move the legs over a whole range of optical steps, in the meantime keeping track of the amount of motor steps it takes a leg to travel one optical step. The results are shown in Figures 4.2 and 4.3.

Again, while not providing a very thorough analysis, we note that the amount of motor steps going into an optical step seems to increase when changing to a 100Ω resistor. This would suggest that the average size of a motor step decreases.

More importantly, Figure 4.3 provides an example of the typical positional dependence of the behaviour of the piezo actuators. Due to the particular design of the hexapod, the piezo being connected to a spring construction, the motor steps, as a function of position, will follow a bathtub curve. When a hexapod leg is around its lowest position(s), the decoupling of the piezo from the spring (and hence the leg) will result in a sharp increase of the amount of motor steps needed to travel one optical step

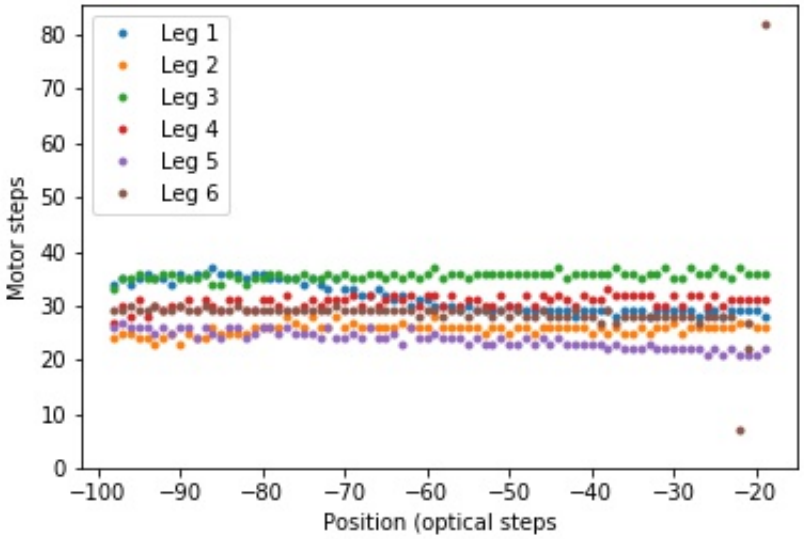

Figure 4.2: *The amount of motor steps per optical step as a function of the leg position for the 18 Ω resistor (a). We applied pulses of 140 V and 200 Hz. This experiment took place around 14 November 2019. (a)*

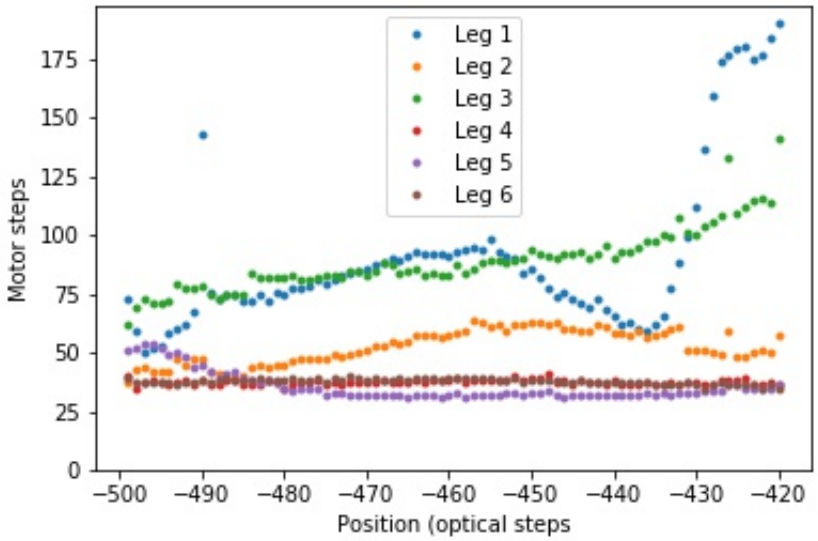

Figure 4.3: *The amount of motor steps per optical step as a function of the leg position for the 100 Ω resistor (b). We applied pulses of 140 V and 200 Hz. This experiment took place around 1 December 2019. (b)*

when trying to reach even lower positions. Pushing this too far can even result in complete decoupling of the piezo and the leg, which one should avoid at all times. Similarly, around the highest positions the piezo actuator is pushing against the limits of its support, resulting in the other steep slope of the bathtub curve. When calibrating the origin, one strives to position it far away from the steep slopes.

While the behaviour of the piezo actuators can be very interesting and enlightening to analyze, we decided to instead focus on the platform movements, which will be discussed in the next chapter.

Chapter 5

Experimental Tests of Platform Movements

We are now ready to check the platform movement equations derived in Chapter 3. We use a Michelson interferometer to determine the z-, θ_x- and θ_y-displacements. To characterize rotations around the z-axis and translations along the x- and y-axes we image an USAF1951 Test Target onto a CCD.

5.1 Interferometric experiments

As discussed in Chapter 2, the Michelson interferometer can be used to measure displacements along the z-axis and rotations around the x- and y-axes with an extremely high accuracy. We use two slightly different experimental setups of the Michelson interferometer, one for the z-displacements and one for the θ_x- and θ_y-displacements.

Before discussing the exact setups, it is worthwhile to go over some of the equipment we used for these experiments. We used the JDS Uniphase 1101/P helium-neon laser at a wavelength of 633 nm for the z-displacement experiment, whereas the Melles Griot Stabilizing 05-STP-903 helium-neon laser, also operating at 633 nm, was used for the θ_x- and θ_y-experiments. In both experiments we made use of the DMK41 BUO2 CCD Camera of The Imaging Source, which has a maximal frame rate of 15 fps and a pixel size of 4.65 μm in both the horizontal and vertical directions. The limitations of both the lasers and the camera will be discussed throughout Sections 5.1.2 to 5.1.4. Lastly, we used two mirrors, highly reflective (T = 0.5%) for wavelengths of 633 nm, of LO Laseroptik GmbH as M_1 and M_2 in the

Michelson interferometer. Note that we also used a mirror of this type as the 45° mirror, as will be discussed in the next section.

5.1.1 Setups

The setup for the measurements along z is shown in Figure 5.1. With this setup we are able to create a circular fringe pattern, as discussed in Chapter 2. We note that the setup used in our experiment is in principle identical to the setup for circular fringes considered there; the mirror M_3 has only been included to deflect the laser beam, which was necessary due to space limitations, whereas the two lenses placed in-between M_3 and the beam splitter simply serve as a collimator to limit the divergence of the laser beam.

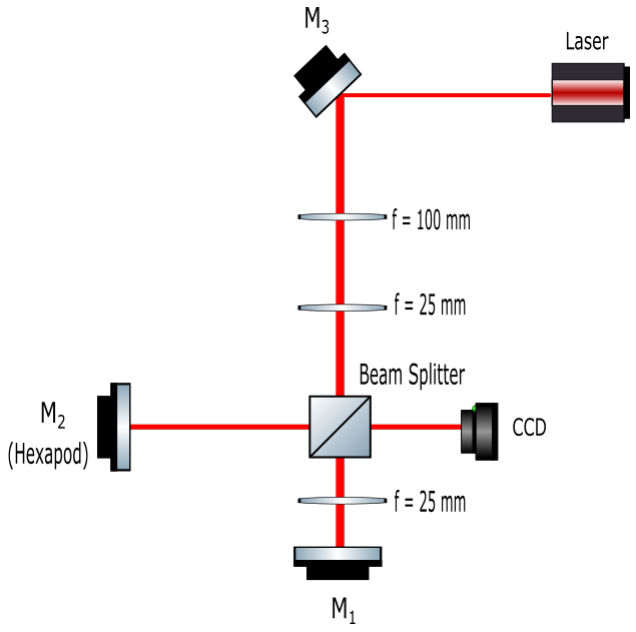

Figure 5.1: *Setup used for the measurement of z-displacements around 7 November 2019. The distance from the beam splitter to M_1 is 12 $\pm$ 0.5 cm, whereas the distance from the beam splitter to M_2 is 25 $\pm$ 1 cm.*

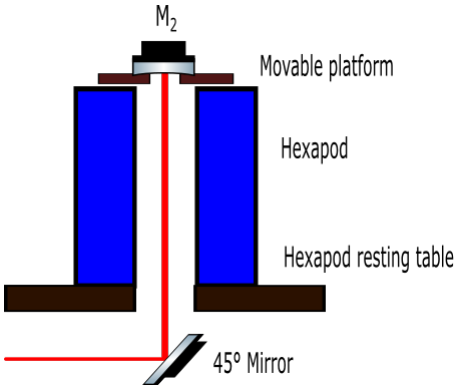

Figure 5.2: *Hexapod setup for the z-, θ_x- and θ_y-experiments. Note that for θ_x and θ_y we use the exact same configuration (same mirrors), only then we place the hexapod in the other arm of the Michelson.*

Having created the circular fringe pattern, we use the CCD to record the changes in this pattern resulting from the movements of the hexapod platform, which contains M_2, in the z-direction. We then analyze how the pixel intensity in the center of the pattern changes as a result of the displacements, and from this we can derive the actual displacement distance, as will be described in Section 5.1.2. Note that the actual size of the ring pattern, which is dependent on the relative positions of the lens in the M_1-arm and the CCD, is irrelevant here; we are only concerned with changes in the pattern.

To ensure that no reflected laser light travels back into the laser, which can negatively affect its performance, we make use of the large distance between M_3 and the beam splitter, which is around 60 cm in our experiment. Even for angles smaller than 0.01 rad between the incident and reflected beams will we then be able to block the reflected light with a screen. It is much easier, however, to use a Faraday isolator, which is what we have done in subsequent experiments.

Before discussing the setup for the θ_x- and θ_y-experiments, we briefly consider the procedure used to ensure that the laser beam travels parallel to the z-axis, as shown in Figure 5.2. We use a special 45 $^\circ$ ($\pm$ 0.1°) mirror mount made by Ruud van Egmond of the Fijnmechanische Dienst to deflect the incoming laser beam towards M_2. Tuning the setup in such a way that the beam reflected from M_2 travels back towards the beam splitter, we are assured that the angle of the beam with respect to the z-axis is smaller than 0.01 rad.

The setup for the θ_x- and θ_y-displacements is shown in Figure 5.3. We use it to create Fizeau fringes, and we observe that this setup is practically

the same as the Fizeau-setup discussed in Chapter 2. The only additions in our setup include a collimator and a Faraday isolator, for reasons already discussed. Furthermore, we note that the hexapod is now located in the M_1-arm of the Michelson interferometer, which was again purely done out of space considerations. For reasons mentioned in Sections 2.1.2 and 5.1.3 we place the hexapod in such a way that the y-axis of the movable platform is aligned with the M_1-arm of the Michelson interferometer. We also ensure that the laser beam reflected from the 45° mirror is again very nearly parallel to the z-axis. Tilting the platform around either the x- or the y-axis will then alter the fringe density, allowing us to determine the angular displacement around said axes.

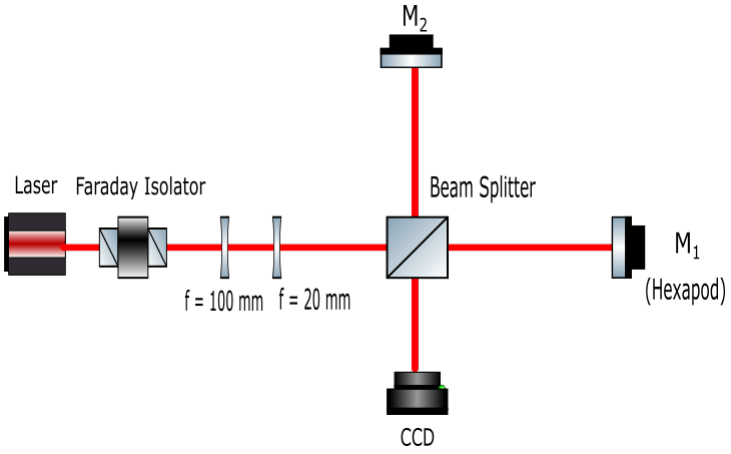

Figure 5.3: *Setup used for the measurement of θ_x- and θ_y-displacements around 16 December 2019. The distance from the beam splitter to M_1 is 51 $\pm$ 1.5 cm, whereas the distance from the beam splitter to M_2 is 49 $\pm$ 0.5 cm*

5.1.2 Displacements in the z-direction

Having built the z-setup, we displace all the legs of the hexapod by a single optical step, followed by a rest period of around six seconds, doing nineteen optical steps in total. This rest period allows us to easily distinguish between consecutive platform displacements, as can be seen from Figure 5.4. We can count the amount of fringes Δm passing through the center by noting that two consecutive peaks in Figure 5.4 correspond with exactly one fringe. We read off Δm within an accuracy of 1/12th of a fringe. We can then calculate the platform displacement using the formula introduced in Section 2.1.1,

$$\Delta z = \Delta m \frac{\lambda}{2}, \tag{5.1}$$

with Δz the platform displacement and λ the wavelength of the laser. Hence in Figure 5.4 we see three consecutive *individual* platform displacements, each with a displacement distance equal to 633 nm. Put differently, we see a *total* displacement of 1899 nm over a range of three steps.

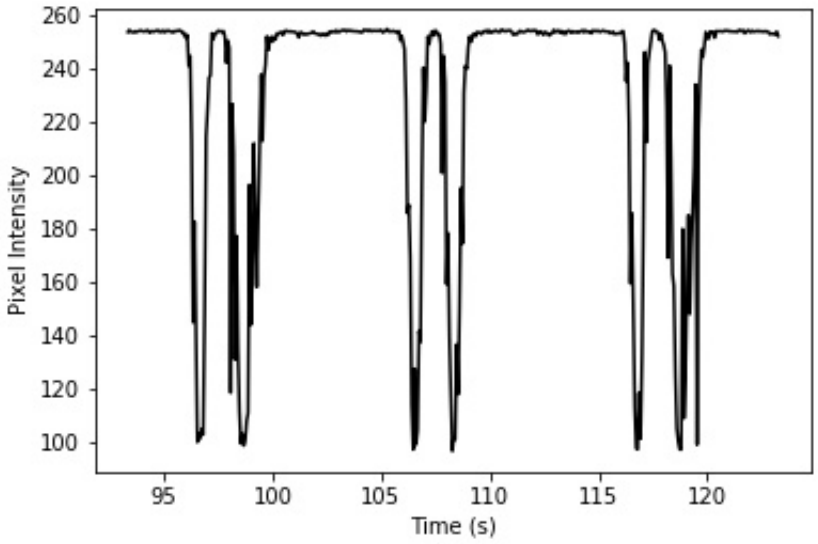

Figure 5.4: *Segment of the measurement for the z-displacements, where we plot the pixel intensity in the center of the interference pattern as a function of time. The rest period is around six seconds, and consecutive platform movements can easily be distinguished from one another. (a)*

A plot over the *whole* range of steps is shown in Figure 5.5. From the linear fit we find the size of a single z-displacement to be equal to 654 $\pm$ 3 nm. Referring to Equation 3.3, with $\sin\varphi = 0.871$, this would suggest an optical step size of 570 nm $\pm$ 3 nm. We should note that that these error bars are purely due to statistics; the actual uncertainty is larger due to systematic errors, as we will see soon.

However, when we look at our original plot of the pixel intensity, we see that ten individual steps, including those shown in Figure 5.4, correspond to steps of 633 nm. Within our reading accuracy of 1/12th of a fringe one then finds these ten steps to have an average z-displacement of 633 nm, within an error of $\pm$ 4 nm. This would in turn imply an optical step size of 551 $\pm$ 4 nm for these steps.

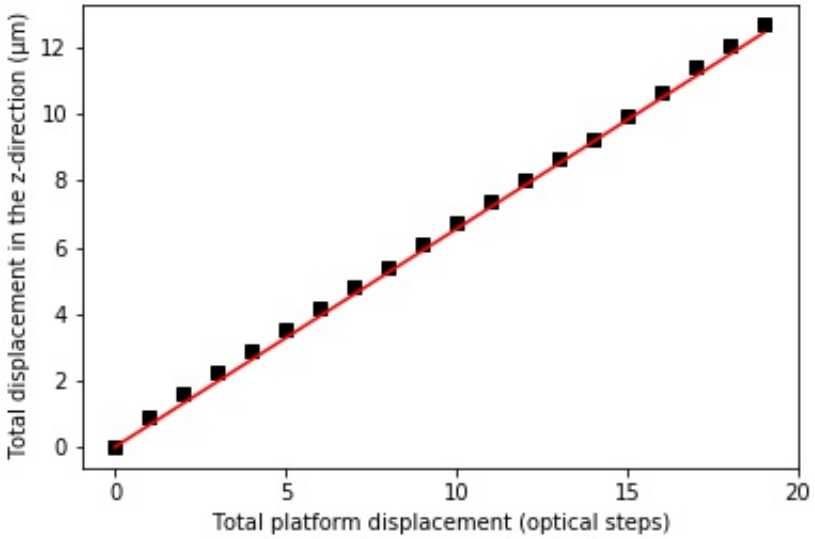

Figure 5.5: *The measured z-displacements, in μm, as a function of the platform displacements, given in optical steps. The slope of the linear fit has a value of 0.654 μm per optical step and a standard error of 0.003 μm per optical step. (a)*

It is very important to determine the causes of this discrepancy. It might simply be the result of noise creeping in during some parts of the measurement, making it more difficult to read off the correct displacement of the other nine steps, as can be seen clearly in Figure 5.6. However, it could also prove to be a more fundamental issue, namely that the optical readers might not be evenly spaced, hence making the optical step size dependent on the exact *absolute* position of the legs. For this reason we will, in the remaining experiments, determine from the experimental data the optical step size which yields the most correspondence with our theoretical predictions. We will refer to this as the *actual* optical step size. Assuming the optical readers are truly evenly spaced and our model is correct, one expects to find a linear relation between the experimental results and the theoretical predictions as well as the same actual step size for all experiments, within their respective errors bars, of course.

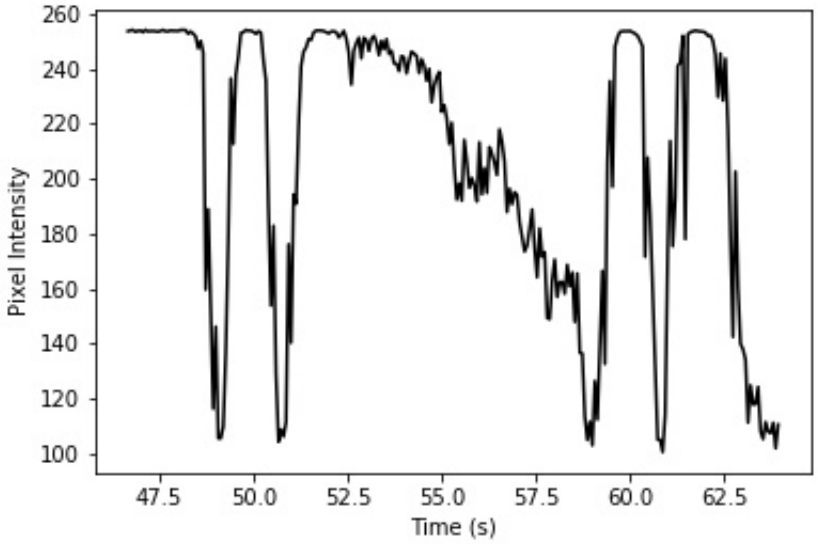

Figure 5.6: *Segment of the measurement for the z-displacements; a plot of the pixel intensity in the center of the interference pattern as a function of time. There appears to be a significant amount of noise, its amplitude being of the same order of magnitude as the signal itself. (a)*

Delving a bit deeper then into the possible sources of the noise, we note that the laser used is not completely frequency-stable, the output frequency changing in a predictable pattern over time. While we only conducted our experiments after the laser had been turned on for a significant amount of time ($>$ 10 minutes), thereby minimizing the frequency fluctuations as much as possible, the length difference of 13 $\pm$ 1 cm between the two arms still made our interferometer susceptible to this effect. As a quantitative example, a frequency change of 1 GHz will result in a shift of about 0.9 fringes in our setup. This problem can easily be avoided by ensuring that the arms of the interferometer are of the same length. As a general rule the arm length difference should be much smaller than the length of the laser. Secondly, we did not take any measures to reduce acoustic vibrations, which could also be a source of noise. In that case, however, we would expect the noise to be present at all times, whereas Figure 5.4 implies that there are significant periods of time in which there is virtually no noise at all during the measurement, at least not of an amplitude comparable to that of our signal.

Since we count a fringe shift of around 2 fringes in the rest periods of our measurements, and a fringe shift of around 38 fringes in the move-

ment periods, we roughly estimate our systematic error (due to drift) to be around 5%, or $\pm$ 29 nm.

Deeming the arm length difference to be the most likely source of noise, we tried to repeat the experiment in December with a frequency-stable laser, the Melles Griot 05-STP-903, with a slightly altered setup. We used the setup of Figure 5.3, with the addition of a lens with a focal length of 40 cm in the M_2-arm.

It should be noted that this experiment took place after the second calibration around the *absolute* leg position (143, 4226, 6466, 1579, 16, 517), with respect to the origin of the *second* calibration. The previous experiment, however, was carried out before this calibration, and somewhere around (-50,-50,-50,-50,-50,-50), with respect to the origin of the *first* calibration. In the new experiment we also increased our stepping range to a thousand optical steps, in order to get as clear as possible an idea of the spacing between the optical readers.

Two slices of this measurements are shown in Figures 5.7a and 5.7b. We were unable, however, to make a plot analogous to Figure 5.5, mainly due to the occurrence of strange behaviour, as shown in Figure 5.7b. In this figure it is rather ambiguous whether we should count these steps as a full fringe shift, or no shift at all. It should be noted that we used voltage pulses of 100Hz (and 100V) on the piezo's here, as opposed to pulses of 10Hz (and 100V), as in the previous experiment. This will result in a hexapod leg travelling a distance of an optical step in a much shorter amount of time. Since our CCD can only take 15 frames per second, the strange behaviour seen in Figure 5.7b is most likely the result of undersampling. Due to time restraints we were unable to continue this research, but it is very important that this will be investigated further in the future. We suggest replacing the current CCD with one which has a frame rate at least a several factors higher, in order to avoid undersampling.

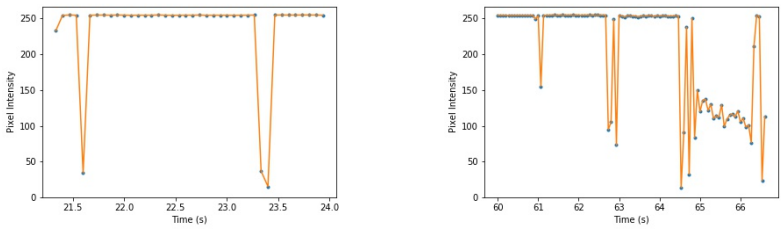

Figure 5.7: *Segments of the measurement for the z-displacements around the absolute platform position of (143, 4226, 6466, 1579, 16, 517); a plot of the pixel intensity in the center of the interference pattern as a function of time. (b)*

5.1.3 Displacements in the θ_x-direction

Before continuing, we note that the θ_x- and θ_y-experiments both took place after the second calibration, around the absolute leg position of (-450,-450,-450,-450,-450,-450).

To accurately measure the rotations about the x-axis, we use the setup as drawn in Figure 5.3. It is important that the mirrors are adjusted in such a way that we have almost completely horizontal fringes, like those shown in Figure 5.8. When this is the case a rotation of the hexapod mirror around the x-axis will only change the distance between consecutive fringes, Δd, but not their orientation. With the hexapod control program to rotate the movable platform around the x-axis and the ImageJ-program to measure the new fringe separation distance, we can find the new angle α between the hexapod mirror and mirror M_2 using the formula introduced in Chapter 2,

$$\alpha = \frac{\lambda}{2\Delta d}, \tag{5.2}$$

where λ is the wavelength of the laser.

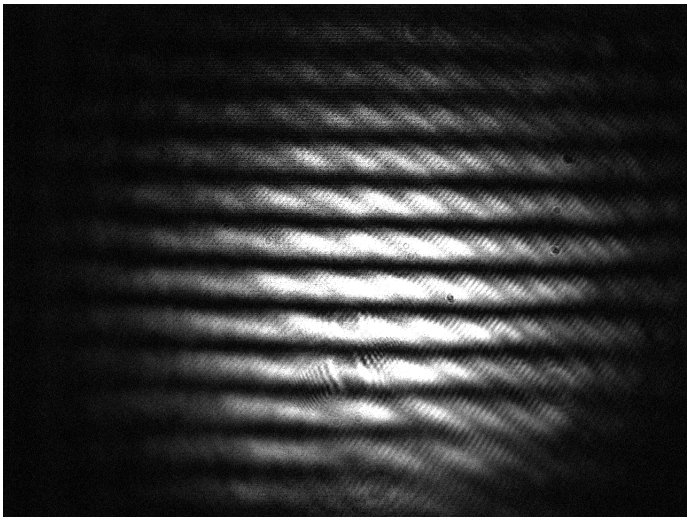

Figure 5.8: *Almost horizontal Fizeau fringes created with the Michelson interferometer during the θ_x-measurements on 16 December 2019. To be more precise, the fringes are slightly tilted, making an angle of -1° with respect to the horizontal. (b)*

By determining α before and after the rotation we can determine the experimentally observed angular displacement, and compare this with the angular displacement as predicted from the movement of the platform.

The results are shown in Figure 5.9. From this figure we find an actual step size of 520 $\pm$ 2 nm. In the next section we will check whether we observe similar behaviour when investigating the rotations around the y-axis.

As for any systematic errors in the measurement, we note that the fringes at the starting point of the measurement, corresponding to the angular displacement of 0 μrad in the computer program, are not perfectly horizontal, but slightly tilted at roughly -0.5° (not the one shown in Figure 5.8!). Notice that we have defined the signs of the angles in accordance with the right hand rule, with the thumb pointing out of the image corresponding to a positive angle, as in Figure 5.8 for instance. The tilt 'decreases' to a minimum of about -11° when moving in the direction of the positive θ_x-displacements, and increases to a maximum of approximately 2° when going towards the negative displacements. By better aligning the mirrors, the accuracy of this experiment can be improved.

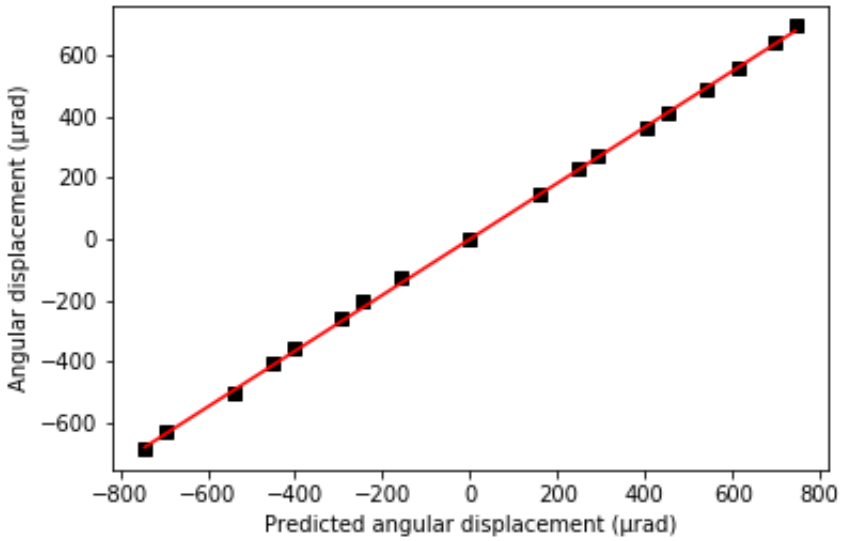

Figure 5.9: *Comparison of the theoretically predicted angular displacements, assuming an optical step size of 570 nm, with the experimentally determined angular displacements for θ_x. The slope of the linear fit has a value of 0.912, with a standard error of 0.004, which indicates that the actual optical step size is 520 $\pm$ 2 nm. (b)*

5.1.4 Displacements in the θ_y-direction

Using an analogous approach as in Section 5.1.3, with the only difference being that we now of course use a vertical fringe pattern, we arrive at the results shown in Figure 5.10. We now find an actual optical step size of 519 $\pm$4 nm. This falls within the limit of the error bars of the θ_x result, which indicates that we can apply the platform displacement equations to calculate the actual displacements for the θ_x- and θ_y-operations.

Similarly to the θ_x-experiment, the fringes here are not completely vertical, the initial tilt being around 1° (with respect to the vertical). This rises up to 8° in the positive direction, and decreases to approximately -4° in the negative direction. Since the tilting angles for θ_y are slightly larger than those for θ_x, this might explain why we also have a slightly larger standard error here.

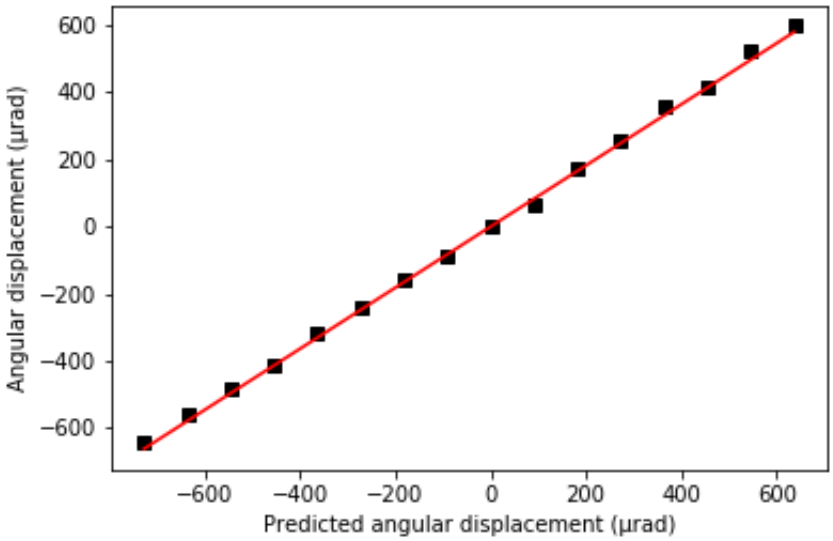

Figure 5.10: *Comparison of the theoretically predicted angular displacements, assuming an optical step size of 570 nm, with the experimentally determined angular displacements for θ_y. The slope of the linear fit has a value of 0.910, with a standard error of 0.007, which indicates that the actual optical step size is 519 $\pm$4 nm. (b)*

5.2 Imaging experiments

5.2.1 Setup

Whereas the displacements along the z-axis and the rotations around the x- and y-axes can easily be measured with the Michelson interferometer, the other 'Cartesian' directions require a different approach. To completely characterize our coordinate set, we build an imaging system as drawn in Figure 5.11. The basic idea of this setup/experiment is relatively straightforward. We place an USAF1951 Test Target, as pictured in Figure 5.12, on the movable platform of the hexapod, and use an aspheric lens with a focal length f of 8 mm to obtain a magnified image of the test target on the camera. Note that we place our camera such that the vertical axis of the camera lens is parallel to the y-axis of the hexapod, so that displacements along the y-axis will be seen as vertical movements in the videos/photos.

The magnification m of the image can be calculated by measuring the image distance s' between the lens and the camera and applying the thin lens equation, $\frac{1}{s} + \frac{1}{s'} = \frac{1}{f}$ with s the object distance between the lens and the USAF target, in conjunction with the magnification formula, $|m| = |-\frac{s'}{s}| = |1 - \frac{s'}{f}|$ [9]. Another way to determine the magnification is by measuring the distance spanned by a line pair (meaning a black and a white line) of the USAF target using the ImageJ-program and comparing this with the known line pair density of that element.

For the x- and y-displacement experiments we measured a distance of 33 ± 1 cm between the lens and the CCD , yielding a magnification of 40 ± 1. Here we have ignored the additional minus sign resulting from the inversion of the image due to the lens. Using the second method, however, we found a magnification of 22.8 ± 0.6. We deem the latter method more reliable, since we did not adequately check whether we truly placed the CCD at the image distance. Based on the result of the second method and the magnification formula, we estimate the actual image distance to be 19 ± 0.4 cm. For the θ_z-displacements we solely relied on the second method, and found a magnification of 12.0 ± 0.1.

Having determined the magnifications, we move the platform along either the x- or y-axis, or rotate it around the z-axis, and record the movement of the USAF Test Target with the CCD-camera, the same as used in the interferometric experiments. Next we calculate the distance travelled by comparing the position of a particular object in the video, for instance a white line, in the first frame with its position in the last frame of the video, where we again make use of ImageJ. We then compare this distance with

the one predicted from the leg displacements of the hexapod, providing an accurate test for our theory.

Before discussing the results, we mention that the x- and y-experiments were both performed around the platform position (-50,-50,-50,-50,-50,-50), and before the second calibration. The θ_z-experiment was performed after the second calibration, around (-450,-450,-450,-450,-450,-450).

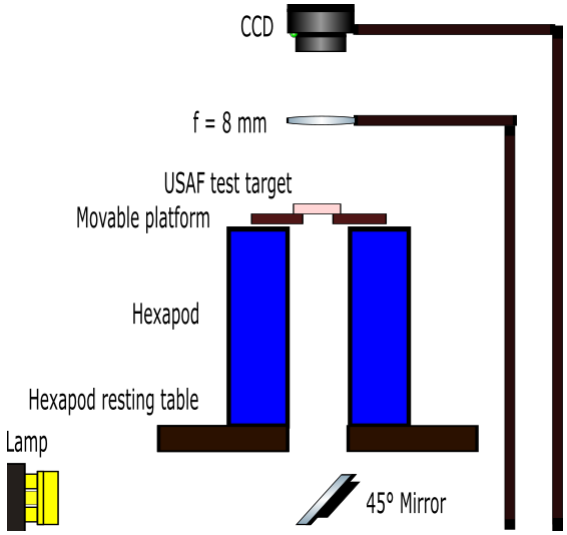

Figure 5.11: *Experimental setup for the measurement of displacements in x, y and θ_z. The experiments for x and y were carried out around 17 November 2019, whereas the θ_z-experiment took place on 28 November 2019*

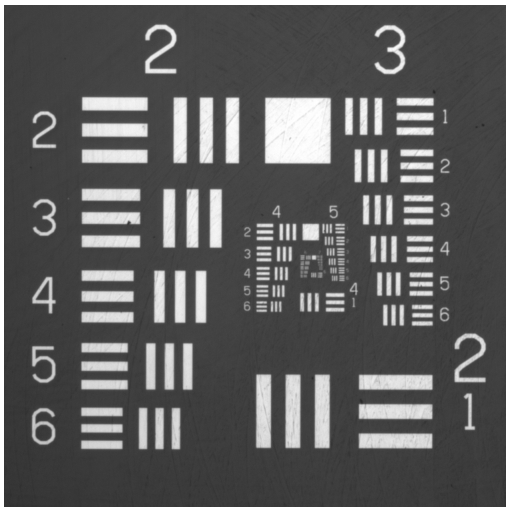

Figure 5.12: *The Thorlabs R1DS1N USAF1951 Test Target.*

5.2.2 Displacements in the x-direction

The results for the movements in the x-direction are shown in Figure 5.13. Note that we perform this experiment with a method somewhat similar to the z-displacement experiment, using only single platform *displacements*, in this case multiples of (-15,15,19,3,-3,-19). Adding the displacements together, just as in Section 5.1.2, we arrive at the given plot.

Using only the data from Figure 5.13 we find an actual optical step size of 683 ± 4 nm. However, the error bar increases when we take into account the inaccuracy of $\pm$ 0.6 in the magnification. By calculating the slopes of the fits corresponding to the magnifications of 22.2 and 23.4 one then finds 683 ± 19 nm.

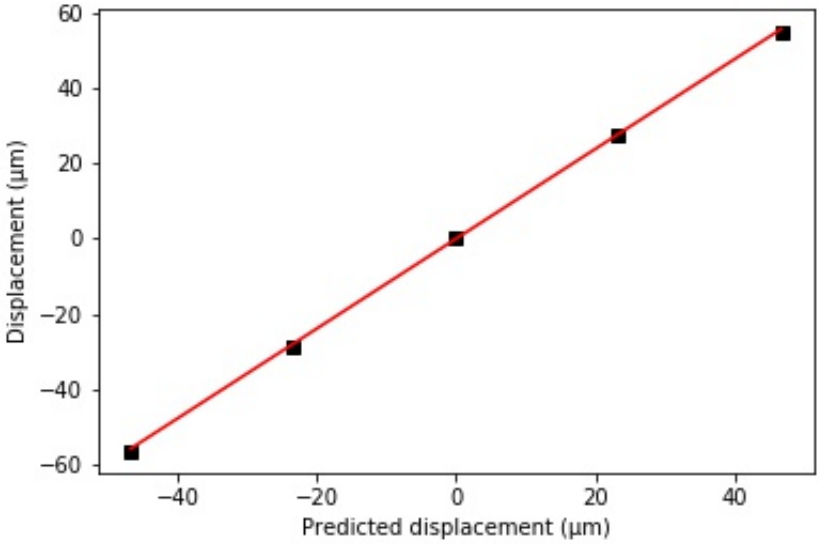

Figure 5.13: *Comparison of the theoretically predicted displacements, assuming an optical step size of 570 nm, with the experimentally determined displacements for x, assuming a magnification of 22.8. The slope of the linear fit has a value of 1.198, with a standard error of 0.007, indicating that the actual optical step size is 683 ± 4 nm. (a)*

We note that this value for the actual optical step size is 30% higher than those for θ_x and θ_y. We want to emphasize again that this experiment took place *before* the second calibration, as opposed to those corresponding to the x- and y-rotations. Since the y-translations took place on the same date and around the same platform position, we deem it more valuable to compare the results of that experiment with the actual step size found

here. If they do not match, we expect there to be a flaw in our platform displacement calculations for x and y.

As for the flaws in our experimental data itself, we first point out that we have taken fewer data points. Adding more data will give a completer characterization of the x-displacements, allowing a more rigorous comparison with our theoretical predictions. Secondly, and of less importance, the platform displacements used do not correspond to pure x-translations, at least from a theoretical point of view. The platform equations predict that a displacement of (-15,15,19,3,-3,-19) will yield slight rotations around the y-axis of about 10 μrad and rotations of 30 μrad around the z-axis. However, since we conducted our experiments only a few micrometers away from the center of the platform, we expect this last issue to have an effect of less than 0.01% on our data. We emphasize again that the impossibility of pure x-,y, θ_x- and θ_y-operations here is purely a result of the leg positions only being able to take on discrete values.

5.2.3 Displacements in the y-direction

The results for the movements in the y-direction are shown in Figure 5.14. The method we use is equivalent to the one described in the previous section, the only difference being that we now use multiples of (13,13,7,-19,-19,7) as our platform displacements.

Again taking into account the uncertainty in the magnification, we find an actual optical step size of 641 $\pm$ 17 nm. We see that this is in disagreement with the results for x. We therefore strongly suspect our calculations for x and y to be flawed.

It should be pointed out that this need not necessarily be the result of the equations corresponding to x- and y-translations being *entirely* incorrect. We analyzed the video of the movements to determine whether the motions were truly along the x- and y-axes. We found an angle of $1.2^\circ \pm 0.8^\circ$ with respect to the x-axis for the x-motion, and an angle of $0.6^\circ \pm 0.7^\circ$ with respect to the y-axis for the y-motion. This would suggest that our movements are along the correct axes, the discrepancy between theory and experiment simply being a matter of disagreement in the distance size. Perhaps different scaling factors need to be added to the x- and y-equations, but we did not delve any further into this matter due to time restraints.

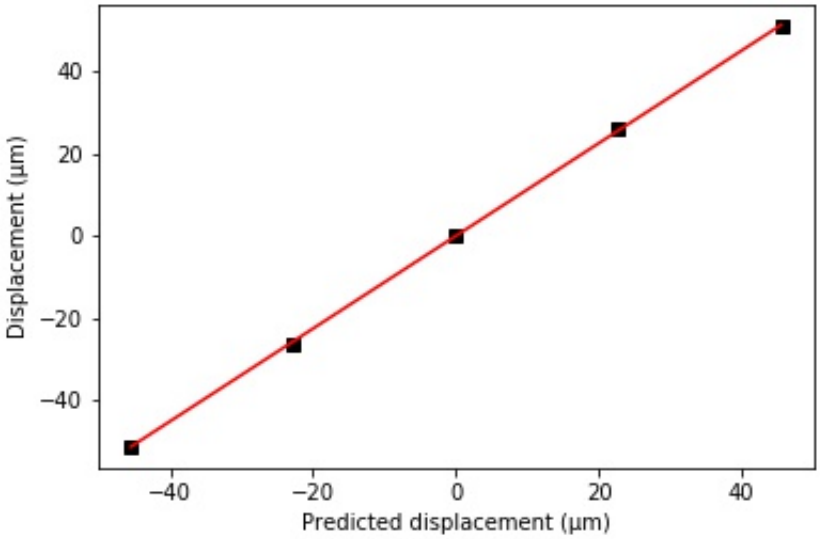

Figure 5.14: *Comparison of the theoretically predicted displacements, assuming an optical step size of 570 nm, with the experimentally determined displacements for y, assuming a magnification of 22.8. The slope of the linear fit has a value of 1.124, with a standard error of 0.006, indicating that the actual optical step size is 641 ± 3 nm. (a)*

5.2.4 Displacements in the θ_z-direction

Unfortunately, we did not manage to obtain useful results for the rotations around the z-axis. We will give a brief summary of the method used, and provide several suggestions for improvement.

Since our aspheric lens has a numerical aperature (NA) of $1/2$, by the Abbe diffraction limit we have a minimum resolvable distance of [13]

$$d = \frac{\lambda}{2NA} = \lambda, \tag{5.3}$$

with the wavelenght λ around 0.5 μm for visible light.

Now, a rotation around the z-axis of $\Delta\theta_z$ will result in an object, for instance a white line, a distance R away from the center of the movable platform being displaced by an amount of $R\Delta\theta_z$. To make the rotations as visible as possible, we choose an element on the USAF Target as far away from the center as possible, in our case Element 6 of Group 3, which is at a radius of 0.16 ± 0.01 mm. As can be seen from Figure 5.15, the rotations are barely visible (large error bar), giving a total displacement 2.3 ± 0.8

pixels which corresponds to 0.89 $\pm$ 0.31 μm. This in turn gives a rotation angle θ_z of 5.6 mrad $\pm$ 2 mrad, which corresponds to an actual optical step size of 310 $\pm$ 110 nm. For these reasons, as well as the very limited amount of *useful* (visible) measurements taken, we deem the results of this experiment to be unreliable.

At the time of these measurements the available platform *position* range was still relatively small, extending from (0,0,0,0,0,0) to (-1000,-1000,-1000,-1000,-1000,-1000), and we were thus not able to produce larger rotations. In our setup then it was also difficult to improve the magnification, for we could only change the position of the lens by hand, which is time-consuming and inaccurate when submillimeter precision is required.

Due to time restraints and differing priorities, we were unable to carry out the experiment properly. We offer two suggestions which can be implemented quite straightforwardly in the setup, as shown in Figure 5.11. First of all, we suggest building a simple system which enables the experimenter to tune the distance between the lens and the platform using micrometer screws. Secondly, it might be helpful to consider the use of another target plate, specifically one where the pattern extends further out of the center.

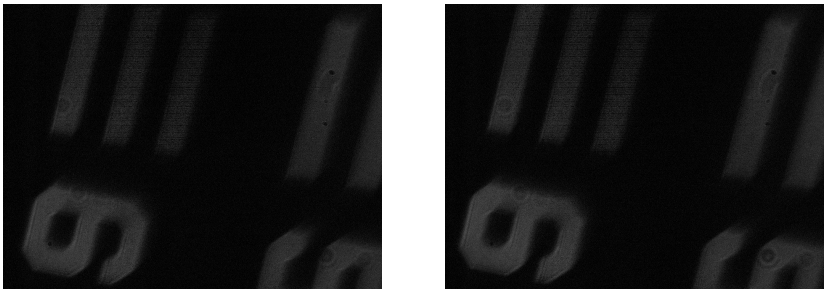

(a) Before the rotation ***(b)*** After the rotation

Figure 5.15: *Platform displacement of (100,-100,100,-100,100,-100), corresponding to a predicted rotation angle in-between 9.71 and 10.14 mrad (optical step sizes of 536 nm and 560 nm respectively). The actual displacement seen in this figure has a magnitude of 2.3 pixels $\pm$ 0.8 pixels. (b)*

Chapter 6

Concluding Discussion and Outlook

While we have made progress by introducing a mathematical model to describe the platform movements and developing a computer program with which we can control the motion of the hexapod, a lot of uncertainties remain. Although our model seems in agreement with the experimental results for θ_x and θ_y, the other coordinates yield less hopeful results. Most importantly, we have very little information about the θ_z-operation. Since we were unable to perform the different coordinate experiments before and after the second calibration, limited statements can be made about the validity of our model.

Further testing is therefore required. We suggest to first fully characterize the optical step size for the range of all available leg positions, using the z-setup (with a frequency-stable laser and equal arm lengths), to test whether the assumption of a constant step size is valid. When this is done, we recommend repeating the discussed experiments to test whether our (idealized) model is truly applicable. Other effects, such as the expected coupling between θ_x and y as well as θ_y and x can then also be tested. To do so, we recommend using the imaging system, and check whether rotations around said axes will result in the coupled translations discussed. Finally, limitations due to design can be tested, yielding then a very accurate characterization of the JPE hexapod.

Bibliography

[1] C. Toninelli and al., *A scanning microcavity for in situ control of single-molecule emission*, Appl. Phys. Lett. **97**, 021107 (2010).

[2] L. Greuter, S. Starosielec, D. Najer, A. Ludwig, L. Duempelmann, D. Rohner, and R. J. Warburton, *A small mode volume tunable microcavity: Development and characterization*, Appl. Phys. Lett. **105**, 121105 (2014).

[3] M. Mader, J. Reichel, T. Hansch, and D. Hunger, *A scanning cavity microscope*, Nature Communications **6**, 7249 (2015).

[4] M. Fox, *Quantum Optics: An Introduction*, Oxford University Press, Oxford, 2006.

[5] H. D. Young and R. A. Freedman, *University Physics with Modern Physics*, 14th ed., Pearson Education, London, 2015.

[6] B. P. Abbott and al., *Observation of Gravitational Waves from a Binary Black Hole Merger*, Physical Review Letters **116**, 061102 (2016).

[7] E. Hecht, *Optics*, 5th ed., Pearson Education, London, 2016.

[8] G. Brooker, *Modern Classical Optics*, Oxford University Press, Oxford, 2003.

[9] F. L. Pedrotti and L. S. Pedrotti, *Introduction to Optics*, 2nd ed., Prentice Hall, Upper Saddle River, New Jersey, 1993.

[10] Y. Kligerman and M. Varenberg, *Elimination of Stick-Slip Motion in Sliding of Split or Rough Surface*, Tribology Letters **53**, 395 (2014).

[11] J. Yi, S. Chang, and Y. Shen, *Disturbance-Observer-Based Hysteresis Compensation for Piezoelectric Actuators*, IEEE/ASME Transactions on Mechatronics **14**, 456 (2009).

[12] J. Fraleigh and R. Beauregard, *Linear Algebra*, 3rd ed., Pearson Education, London, 2014.

[13] S. Lipson, H. Lipson, and D. Tannhauser, *Optical Physics*, Cambridge University Press, Cambridge, 1998.

Appendix A

Additional Figures for Platform Displacements

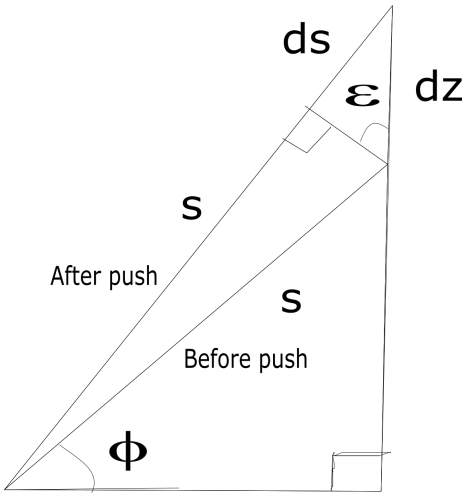

Figure A.1: *Geometry for the translation along z. Due to the joint construction of the hexapod a leg will slightly tilt when pushed upon by the motor, as drawn in the figure. Assuming a small tilt, one has $\epsilon = \varphi$, from which the z-equation follows directly.*

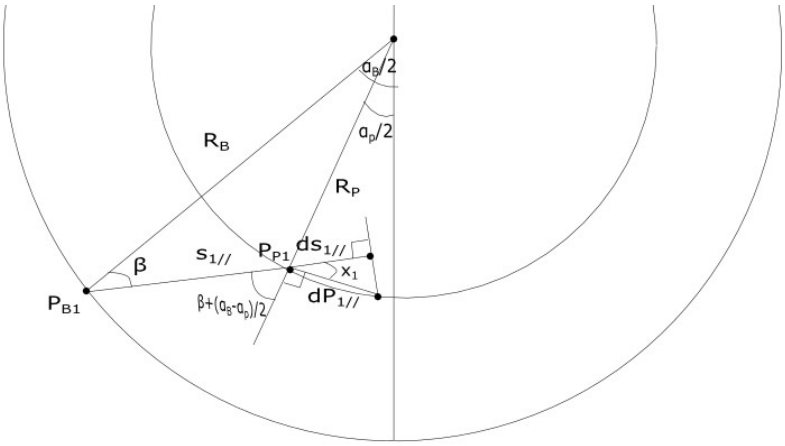

Figure A.2: *Geometry for the rotation around z. In the small angle approximation of our model $dP_{1//} = R_P d\theta_z$.*

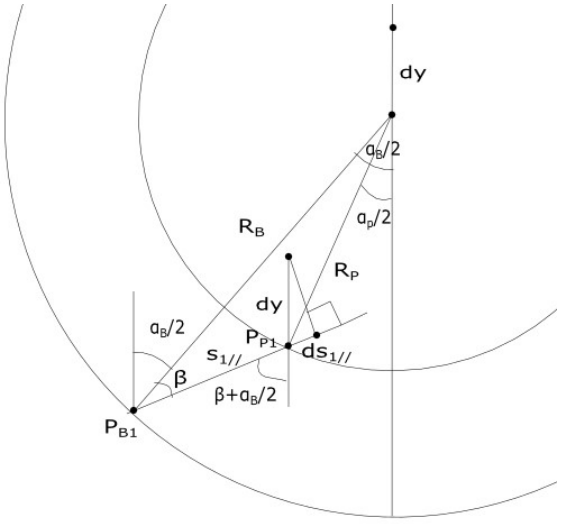

Figure A.3: *Geometry for the translation along y for leg 1. The y-equation for leg 1 follows directly from the triangle with sides dy and $ds_{1//}$. Similar figures can be drawn for the other legs.*

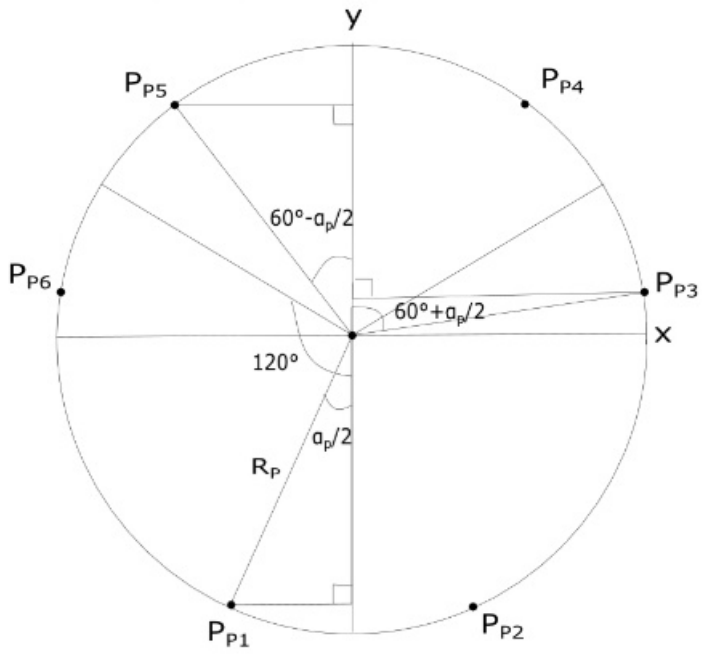

Figure A.4: *Geometry for the rotation around y. In the small angle approximation, there is only out-of-plane movement. Then $ds_{i\perp} = R_{Yi}d\theta_y$, where R_{Yi} is the distance from P_{Pi} to the y-axis.*

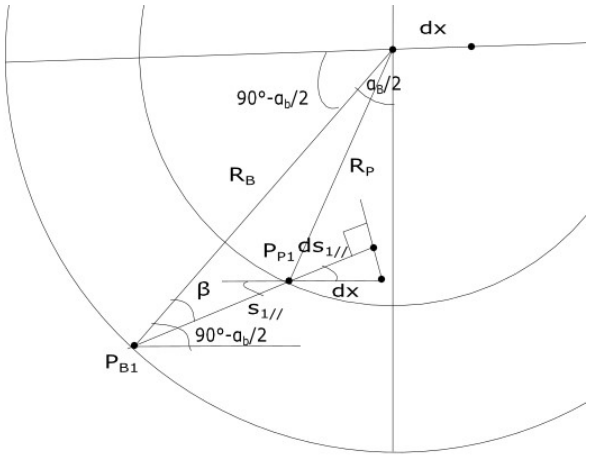

Figure A.5: *Geometry for the translation along x for leg 1. The x-equation for leg 1 follows directly from the triangle with sides dx and $ds_{1//}$. Similar figures can be drawn for the other legs.*

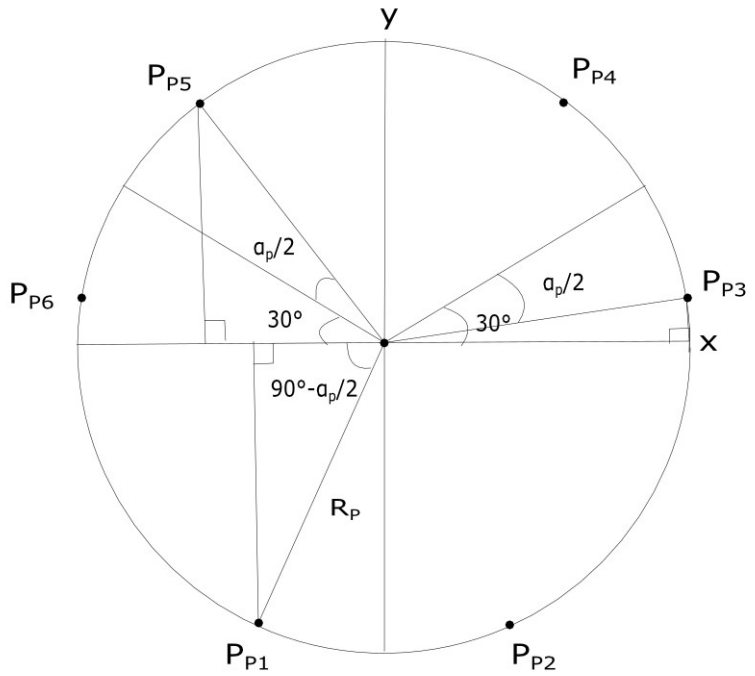

Figure A.6: *Geometry for the rotation around x. In the small angle approximation, there is only out-of-plane movement. Then $ds_{i\perp} = R_{Xi}d\theta_x$, where R_{Xi} is the distance from P_{Pi} to the x-axis.*